ELSEVIER

Journal of Power Sources 81–82 (1999) 472–479

JOURNAL OF POWER SOURCES

www.elsevier.com/locate/jpowsour

Capacity fading of $Li_xMn_2O_4$ spinel electrodes studied by XRD and electroanalytical techniques

D. Aurbach [a,*], M.D. Levi [a], K. Gamulski [a], B. Markovsky [a], G. Salitra [a], E. Levi [a], U. Heider [b], L. Heider [b], R. Oesten [b]

[a] *Department of Chemistry, Bar-Ilan University, Ramat-Gan 52900, Israel*
[b] *Merck, 250 Frankfurterstr., 64290 Darmstadt, Germany*

Abstract

$Li_xMn_2O_4$ spinels were synthesized in different ways, leading to different particle morphologies and different electrochemical behavior. Two types of $Li_xMn_2O_4$ electrodes comprised of active mass synthesized in two different ways were investigated in a standard solution (ethylene carbonate–dimethyl carbonate 1:3/$LiAsF_6$ 1 M) using X-ray diffraction technique (XRD) in conjunction with a variety of electroanalytical techniques. These included slow scan rate cyclic voltammetry, chronopotentiometry, impedance spectroscopy and potentiostatic intermittent titration. We discovered two types of capacity fading mechanisms. One involves the formation of a new, less symmetric and more disordered phase (compared with the pristine $Li_xMn_2O_4$ materials) during the first Li deinsertion reaction of a pristine electrode in the 3.5–4.2 V (Li/Li^+) potential range. This new phase, although inactive, has no detrimental effect on the kinetics of the remaining active mass. Another capacity fading mechanism occurs at > 4.4 V (Li/Li^+) potential and involves dissolution of Mn into the solution, and a pronounced increase in the electrode's impedance. It appears that dissolution of Mn at elevated potentials is connected with degradation of the solution, which also occurs at these potentials at low rates.

Keywords: $Li_xMn_2O_4$; Spinel electrode; XRD

1. Introduction

One of the most important cathode materials for Li ion batteries is $Li_xMn_2O_4$ spinel. This material is relatively cheap, environmentally friendly and may possess a charge density of about 140 (mA h)/g at a potential around 4 V vs. Li/Li^+ [1].

During recent years, a huge amount of work has been devoted to this material and its derivatives. A large variety of preparation procedures was developed, and the correlation between the various synthetic modes and the performance of the materials as practical cathodes in Li ion batteries was investigated [1–3]. Of special importance are the many derivatives of $Li_xMn_2O_4$ that were developed recently, most of them having the formulae $Li_xMn_{2-x}M_xO_4$ (M = Cr [4], Ni [5], Cu [6], Al [7], and even Li atoms that replace Mn atoms in the lattice [8]). Most of these derivatives also have the spinel structure. The substitution of parts of the Mn atoms in the lattice by other metals may increase the stability of these materials [4,5,8], or their operational voltage [6], usually on the account of capacity [4–8]. A great problem with these materials is their stability and reversibility during prolonged charge–discharge (Li deinsertion–insertion) cycling.

There are several comprehensive reports on the study of capacity fading mechanisms for these materials [9,10]. It appears that pronounced, or even slight, structural changes of these materials upon cycling can be one of the reasons for their capacity fading. Another reason may relate to some dissolution processes and/or degradation of the electrolyte solution. It is clear from the literature that there is a complicated relationship between the electrochemical characteristics of these materials and their structure, with a strong impact of the preparation procedure on this relationship. One of the most important challenges in the field of Li ion batteries is to understand possible capacity fading mechanisms of $Li_xMn_2O_4$-based materials and to develop reliable methods for the mass production of stable and reproducible materials. In this work, we report on the study of the electrochemical behavior and capacity fading

* Corresponding author. Tel.: +972-3-531-8317; Fax: +972-3-535-1250; E-mail: aurbach@mail.biu.ac.il

0378-7753/99/$ - see front matter
PII: S0378-7753(99)00204-9

mechanisms of two types of $Li_xMn_2O_4$ spinel materials. We used, simultaneously, fast and slow scan rate cyclic voltammetry (SSCV), potentiostatic intermittent titration (PITT), and impedance spectroscopy (EIS), in order to characterize the electrochemical behavior of the cathode materials. An in situ and ex situ X-ray diffraction technique (XRD) was used for structural characterization.

2. Experimental

We studied two different types of spinel materials denoted as $Li_xMn_2O_4$ A and B. The former was prepared from a mixture of LiOH and MnO_2, which was heated for 40 h at 750°C, and was then allowed to cool slowly to room temperature. $Li_xMn_2O_4$ B was prepared from a mixture of Li_2CO_3 and MnO_2, which was calcined twice at 750°C (18 h period), and was then allowed to slowly cool to room temperature. The MnO_2 used for the synthesis is one of Merck's products.

The surface area of these materials was obtained by the BET method (Gemini 2375 from Micromeritics, USA) and their morphology was studied by SEM (Fig. 1a and b). It appears that $Li_xMn_2O_4$ A consists of irregular particles (0.5–10 μm) of an average surface area of 0.8 m^2/g. $Li_xMn_2O_4$ B consists of large spherical particles (10–60 μm) which are conglomerates of much smaller particles (0.1–1 μm), average surface area of 2.9 m^2/g. The average effective diameters of the particles (which are important for the calculation of the diffusion coefficient) were estimated as 2.4 and 0.5 μm for $Li_xMn_2O_4$ A and B, respectively. From XRD measurements, it was found that the cubic spinel cell units for $Li_xMn_2O_4$ A and B are 8.239 Å and 8.237 Å respectively. Element analysis (EDAX, XPS and atomic absorption of Mn and Li from acidic aqueous solutions in which $Li_xMn_2O_4$ samples were dissolved) showed that while the stoichiometry of pristine spinel B is $LiMn_2O_4$, the stoichiometry of pristine spinel A is close to $Li_{1.045}Mn_{1.995}O_4$.

Thin and thick electrodes were prepared as described [11–13] from the active mass, carbon black (conductive material, 10% by weight) and PVDF binder, 5% by weight) using aluminum foil or a grid as the current collector. These electrodes were tested in two- or three-electrode cells vs. Li or lithiated graphite counter electrodes (Li was used as a reference electrode). The application of SSCV, PITT, EIS and XRD for composite Li intercalation electrodes, and the relevant data analysis, has already been described [11,12]. We used standard solutions comprised of 1:3 EC and DMC (Merck, Tomiyama), and $LiAsF_6$, all Li battery grade (highly pure quality) (FMG).

3. Results and discussion

As already known, $Li_xMn_2O_4$ spinel based cathodes are characterized by two redox processes around 4.0 and 4.1 V (Li/Li^+) appearing as two sets of peaks in their SSCV, and plateaus in their chronopotentiograms [1–8]. Fig. 2 compares the charge capacity of $Li_xMn_2O_4$ A and B during galvanostatic cycling in the 3.3–4.3 V (Li/Li^+) range at C/10 (≈ 2.5 mA/0.2 g of active mass).

Fig. 3 shows the first cycling and a few consecutive SSCV (20 μV/s) of the $Li_xMn_2O_4$ A and B electrodes

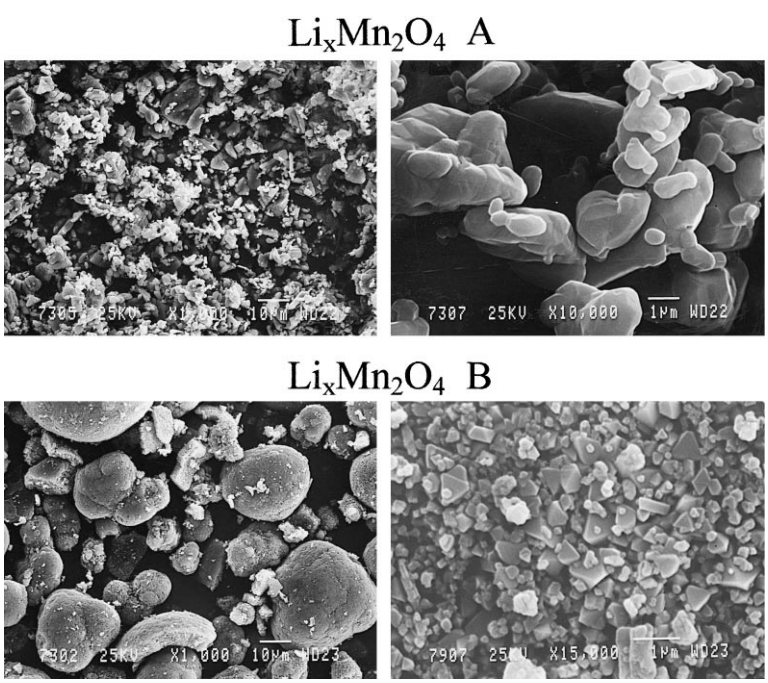

Fig. 1. SEM micrographs showing the particles of $Li_xMn_2O_4$ A and B as indicated. A scale appears in each picture.

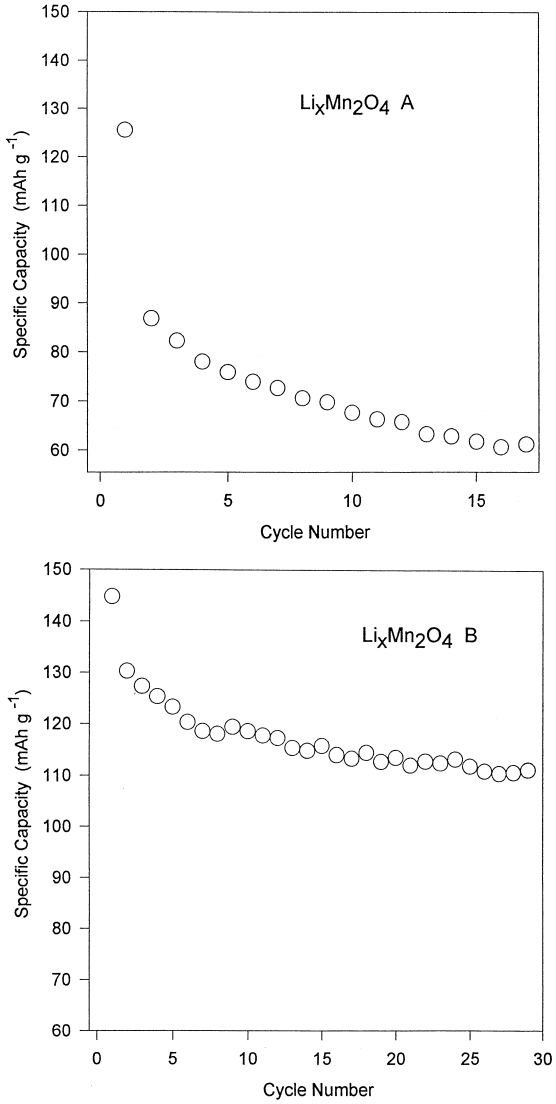

Fig. 2. Charge vs. cycle number for the electrode studies during their galvanostatic cycling in the potential range 3.3–4.3 V (Li/Li$^+$) at $C/10$ rate. (a) $Li_xMn_2O_4$ A; (b) $Li_xMn_2O_4$ B.

(Fig. 3a,b, respectively). These voltammograms clearly show that the voltammetric behavior of $Li_xMn_2O_4$ A electrodes is characterized by relatively high anodic (oxidation) currents at high potentials (>4.2 V, compared with that of $Li_xMn_2O_4$ B electrodes).

Fig. 4 compares the charge vs. potential (E) involved in the first and consecutive SSCV of these electrodes (as indicated). The charge involved is marked in the figure. These three figures show clear trends.

(a) The initial specific capacity of $Li_xMn_2O_4$ B is slightly higher than that of $Li_xMn_2O_4$ A.

(b) Both materials lose capacity after the first cycle.

(c) While the capacity loss for $Li_xMn_2O_4$ B in the first cycle is very moderate (5–6%), it is very pronounced for $Li_xMn_2O_4$ A (31%). From these studies it can be suggested that the major capacity loss for $Li_xMn_2O_4$ A occurs in the process around 4 V (the first plateau which appears during deintercalation). Hence, from these results it appears that $Li_xMn_2O_4$ A is subjected to a capacity fading that probably relates to its initial deintercalation process.

When looking at the voltammetric and the chronopotentiometric data of these two spinel materials, we assume that there is a capacity fading mechanism which is unique to the $Li_xMn_2O_4$ A material, perhaps because of its preparation mode and the resulting morphology. Hence, it was important to understand this fading mechanism in order to be able to correlate such a mechanism to the structure, morphology and preparation mode of $Li_xMn_2O_4$ materials.

Fig. 5 compares XRD patterns (measured ex situ) of pristine and cycled $Li_xMn_2O_4$ A electrodes. The XRD pattern of the cycled electrode is very different from that

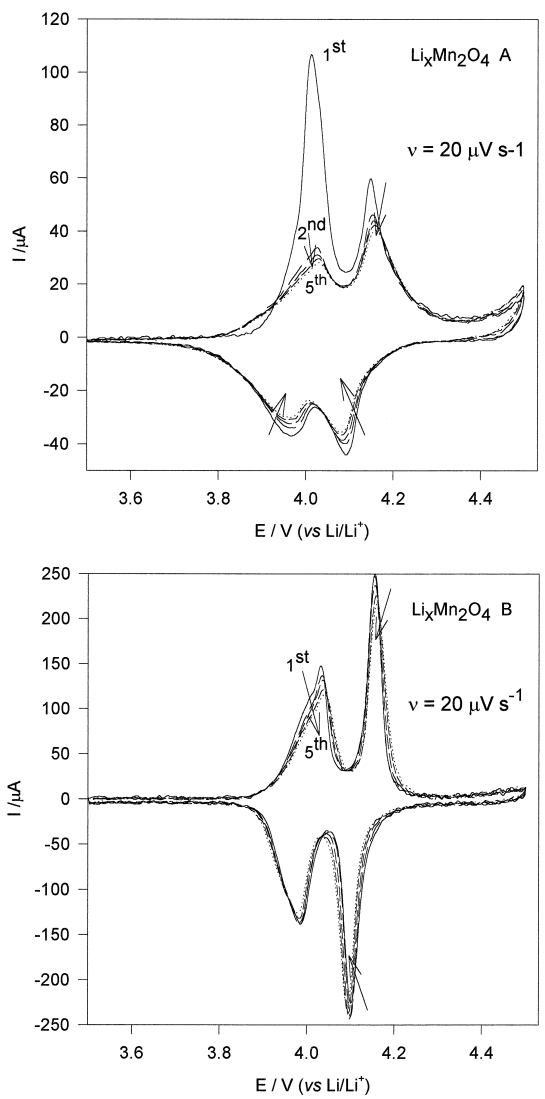

Fig. 3. Several consecutive slow scan CV of the $Li_xMn_2O_4$ electrodes. Scan rate = 20 μV/s. Potential range = 3.5–4.5 V (Li/Li$^+$). (a) $Li_xMn_2O_4$ A electrode, 1.6 mg of active mass/3 cm^2. (b) $Li_xMn_2O_4$ B electrode, 2.6 mg of active mass/3 cm^2.

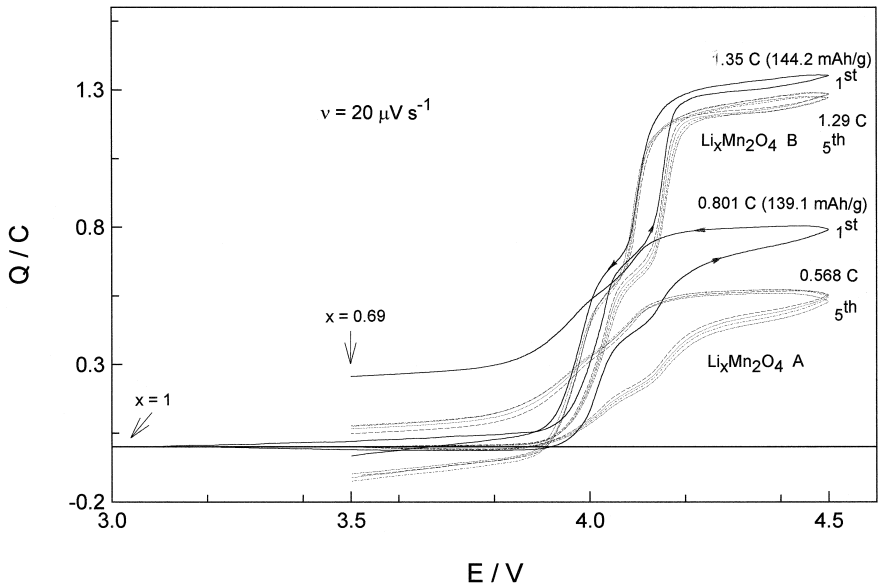

Fig. 4. The cumulative charge involved in consecutive SSCV of the $Li_xMn_2O_4$ electrodes (related to Fig. 3). (a) $Li_xMn_2O_4$ A electrode. (b) $Li_xMn_2O_4$ B electrode. The relevant capacities per gram are indicated.

of the pristine one. The major peaks are broader, less intense, and new peaks appear in patterns related to cycled electrodes. Further rigorous studies of these electrodes by in situ XRD (beyond the scope of this paper) revealed that new XRD peaks appear *irreversibly* in the patterns of $Li_xMn_2O_4$ A electrodes during the first and second cycles in the 3.8–4.2 V (Li/Li^+) range. In contrast, the change in the XRD patterns of $Li_xMn_2O_4$ B electrodes due to cycling is very minor, as demonstrated in Fig. 6. The major XRD peaks appearing in the patterns of pristine and cycled electrodes are very similar, the only difference being that the peak intensity is slightly lower for the cycled electrode (compared with the pristine one).

Extensive ex situ and in situ XRD measurements of these materials revealed that the insertion/deinsertion processes reflected by SSCV and chronopotentiometry relate to phase transitions. XRD measurements at small potential intervals clearly showed that during Li intercalation, the peaks of the Li depleted phase become smaller and new peaks of the Li-rich phase appear. At certain potentials, both sets of peaks coexist and then, as intercalation proceeds, only the XRD peaks of the Li-rich phase appear. This behavior is typical of a reversible electrode, as would

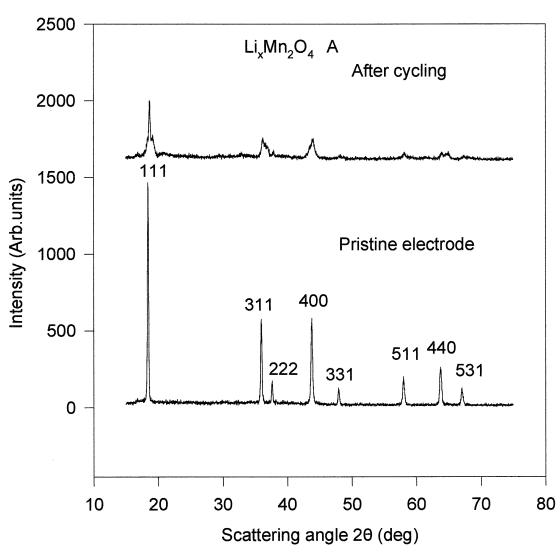

Fig. 5. XRD patterns (obtained ex situ) of $Li_xMn_2O_4$ A electrode in its pristine state (lower pattern) and after prolonged galvanostatic cycling (upper pattern).

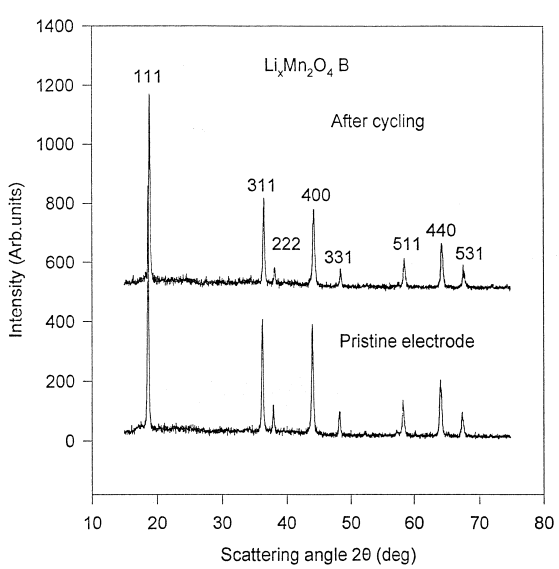

Fig. 6. Same as in Fig. 5 $Li_xMn_2O_4$ B electrode.

be expected for $Li_xMn_2O_4$ B from the electrochemical measurements described above (Figs. 2–4). We investigated the possibility that the capacity fading of the spinel A electrodes is also connected with dissolution of manganese into the solution in addition to the above described structural changes (reflected by the XRD studies).

The graphite electrodes which were used as counter electrodes in the test cells were studied by EDAX. If Mn compounds dissolve into the electrolyte solutions, it is expected that the manganese in the solution should be reduced at the anode and should precipitate as metallic manganese on its surface. The effect of the applied potential was also investigated in this respect.

The following results were obtained from these studies.

Cycling both $Li_xMn_2O_4$ A and B at the potential range from 3.5 V–4.2 V caused no precipitation of Mn on the graphite counter electrodes. We did not find any evidence for Mn dissolution upon cycling or prolonged polarization of $Li_xMn_2O_4$ B electrodes up to 4.5 V (Li/Li^+).

Polarizing $Li_xMn_2O_4$ A electrode to 4.5 V at a slow rate ($C/50$ h) galvanostatically, resulted in a plateau around 4.4 V which relates to a charge which is twice the expected reversible capacity of these electrodes.

Examining the graphite counter electrode in the cell by EDAX revealed that it contains pronounced amounts of surface manganese. The Mn peaks were of the same intensity as the arsenic peaks which belong to the salt reduction products [14]. It is known that the electrolyte $LiAsF_6$ is reduced on graphite to LiF and Li_xAsF_y species [14]. Hence, the high relative intensity of the Mn peaks obviously reflects a destruction mechanism of $Li_xMn_2O_4$ A at high potentials, which involve dissolution of manganese. This mechanism, however, is not relevant to the capacity fading mechanisms which occur around 4 V and relate to structural changes of the material (as described above).

However, it was interesting to discover that when the $Li_xMn_2O_4$ A electrodes were cycled in the potential range 3.8–4.5 V (Li/Li^+) at high rates ($> C/5$ h), the dissolution of manganese was much less pronounced than the slow polarization processes described above. (EDAX spectra of graphite counter electrodes from the fast cycling experiments showed very weak Mn peaks whose intensity was about 5% of the As peaks' intensity).

The fact that pronounced Mn dissolution at high potentials occurs mostly during a slow process may reveal that this process relates to an oxidation of the solution.

We studied the anodic stability of EC–DMC solutions using cyclic voltammetry combined with in situ FTIR spectroscopy [15]. It appears that the onset of these solutions' oxidation may be as low as 3.7 V. However, the oxidation process is very slow over a wide range of potentials (3.7–4.2 V vs. Li/Li^+). Hence we speculate that when the $Li_xMn_2O_4$ electrodes are cycled slowly enough, the slow oxidation processes of the solution produces a sufficient concentration of Lewis acids which interact with the active mass and lead to its partial dissolution.

Thus we have two different degradation mechanisms. The one near 4.4 V is close to that reported by Gao and Dahn [16] and Guyomard and Tarascon [17]. (Note that with spinel B no degradation was observed). The second one, which causes a drastic decrease of the capacity along the 4.0 V plateau for the $Li_xMn_2O_4$ A electrodes, has not been previously described.

The second mechanism occurs around 4 V. As Fig. 4 shows, about one-third of the Li content present in $Li_xMn_2O_4$ A becomes inaccessible during the first cycle.

As follows from the XRD patterns, the new phase formed upon cycling $Li_xMn_2O_4$ A has a lower degree of symmetry compared with the cubic one (two new peaks appear instead of one for the cubic phase). The picture of the two-phase transitions with the old phases (along the 4.0 and 4.1 V plateaus, accounting for about two thirds of the theoretical capacity) is essentially the same as with spinel B. The difference is that the intensity of the peaks for $Li_xMn_2O_4$ A is much less than that for $Li_xMn_2O_4$ B.

We assume that during the first cycling of $Li_xMn_2O_4$ A, a less symmetric and disordered phase is formed near the particle's surface. Hence, the loss of one-third of the capacity of this material during the first cycle is because the new phase is inactive and also masks the active mass (as it is located near the particles' surface). This masking influences both the XRD patterns (decrease in the intensity of the XRD peaks of the active mass), and probably the kinetics of the electrodes.

Moreover, it is quite possible that the pronounced decrease in the capacity of the $Li_xMn_2O_4$ A electrodes observed is not only due to a massive formation of the new phase, but rather because it badly affects the electrode's kinetics.

Important and useful tools for comparing and analyzing the kinetics of Li insertion electrodes are impedance spectroscopy and PITT (from which the diffusion time and the chemical diffusion coefficient of Li into the active mass can be calculated).

Fig. 7a and b present families of Nyquist plots measured at different potentials during Li deintercalation from $Li_xMn_2O_4$ A and B electrodes, respectively. The base potentials at which the electrodes were equilibrated before each measurement are indicated.

The trend in both figures is similar, and it seems that the impedance spectra measured from these two electrodes reflect similar sets of time constants. All the spectra contain a high frequency semicircle which is basically potential invariant. As discussed in Ref. [13], $Li_xMn_2O_4$ electrodes, as well as other Li insertion electrodes (e.g., carbons, $LiNiO_2$, $LiCoO_2$), are covered by Li^+ ion conducting surface films. One obvious source of these films seems to be a reaction between the lithiated compounds and CO_2 from the air, which covers the active mass with Li_2CO_3 films.

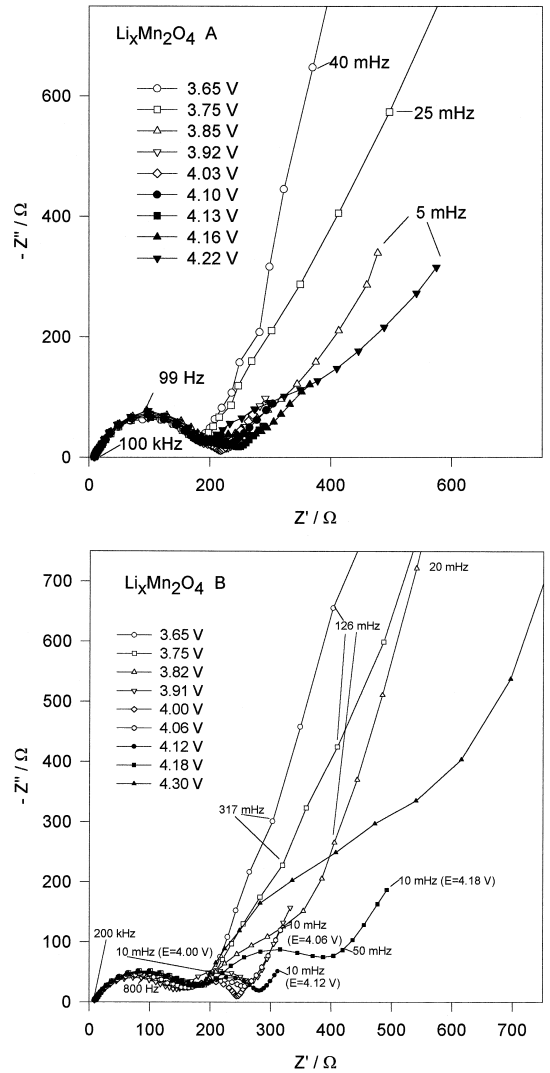

Fig. 7. Impedance spectra (Nyquist plots) obtained from $Li_xMn_2O_4$ A (a) and $Li_xMn_2O_4$ B (b) at different potentials as indicated (100 kHz > ω > 0.005 Hz). The electrodes were equilibrated at each potential before the measurement was carried out. Note the formation of a second, low frequency semicircle at a potential close to the CV peak potentials (Fig. 3), and the fact that at the CV peak potentials Z'' at the lowest frequency (last point in the curve, 0.005 Hz) has a minimum.

Hence, we attribute the high frequency semicircle appearing in the spectra of Fig. 7 to Li^+ ion migration through these surface films, coupled with film capacitance. As shown in Fig. 7, at certain potentials, another low frequency semicircle is developed. In Fig. 8, the diameters of these low frequency semicircles are plotted as a function of the potential for both $Li_xMn_2O_4$ A and B electrodes. The semicircles are very big at potentials below 3.9 V and above 4.2 V (Li/Li^+) and are minimal at the potentials of the CV peaks (i.e., at the potentials of the phase transitions around 4, and 4.1 V vs. Li/Li^+).

As already discussed [13], we attribute this semicircle to charge transfer at the interface between the surface films and the active mass, coupled with the interfacial capacitance.

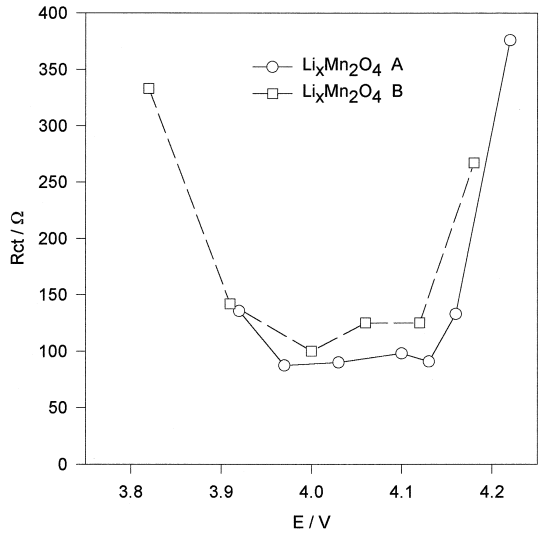

Fig. 8. The diameter of the second, low frequency semicircle appearing in the impedance spectra as a function of the applied potential. The relevant curves for $Li_xMn_2O_4$ A and B are indicated. As explained in the text, we attribute the diameter of this semicircle to R_{CT}.

At the very low frequencies, the spectra of Fig. 7 are characterized by a Warburg-type element which reflects the solid state diffusion of Li into the active mass [13]. At the lowest frequency of the measurements (the mHz region), the Z'' vs. Z' plots become steep lines which reflect capacitive behavior. This capacitive behavior simply relates to the intercalation capacity of the electrodes, which is strongly potential dependent (see the SSCV of Fig. 3).

C_{int} is equal to $1/\omega Z''$ at $\omega \rightarrow 0$. Indeed, at the CV peak potentials, the Z'' measured at the lowest frequencies are minimal. This correlates well with the maxima of C_{int} vs. E at the CV peak potentials.

Hence, it appears from Figs. 7 and 8 and the related data that the impedance behavior of pristine $Li_xMn_2O_4$ A and B electrodes polarized in the range of 3.5–4.2 V (Li/Li^+) is similar in spite of the pronounced difference

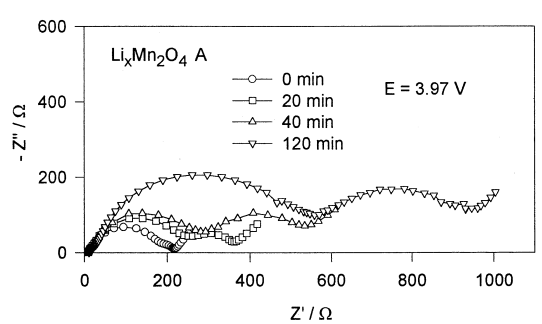

Fig. 9. Impedance spectra (Nyquist plots) measured from $Li_xMn_2O_4$ A electrodes polarized during different periods of time at 4.5 V (Li/Li^+) as indicated. The electrodes were then intercalated with Li until reaching 3.2 V (Li/Li^+) and then were deintercalated up to 3.97 V and measured after reaching equilibrium at this potential.

Table 1
Data extracted from the impedance spectra of Fig. 10 ($Li_xMn_2O_4$ A electrode measured at 3.97 V after being polarized at 4.5 V discharged to 3.2 and then charged to 3.97 V)

Polarization time at 4.5 V (Li/Li^+) [min]	High frequency semicircle (Li ion migration in the surface films)		Low frequency semicircle (charge transfer)		Z'' at $\omega = 5$ mHz
	[a]R_{film} [Ω]	[b]C_{film} [μF]	[a]R_{CT} [Ω]	[B]$C_{intercalation}$ [mF]	
0	171.9	9.83	78	0.72	50.9
20	233.2	8.93	165	1.12	75.9
40	261.6	10.3	319	2.14	113.8
120	518.8	10.8	473	2.3	160.5

[a]R was calculated from the diameter of the semicircles.
[b]C was estimated from ω_{max} of the semicircles as $\omega_{max} = 1/R \times C$ for ideal Randel's circuit.

in their behavior in terms of the capacity loss during the first cycle. This may indicate that the capacity loss of the $Li_xMn_2O_4$ A electrode during the first cycle is due to structural changes in the active mass which deactivate part of it without pronouncedly affecting the kinetics of Li insertion into the remaining (about two-thirds) active mass.

However, the other capacity fading mechanism of the $Li_xMn_2O_4$ A which occurs around 4.4 V affects the impedance behavior of this electrode quite differently.

Fig. 9 shows Nyquist plots obtained from a $Li_xMn_2O_4$ A electrode polarized to 4.5 V for different periods of time, then discharged to 3.2 V, recharged to 3.97 V (the first CV peak potential), equilibrated and measured.

Table 1 presents some data extracted from the spectra of Fig. 10 as a function of the polarization time at 4.5 V (Li/Li^+).

As demonstrated clearly in Fig. 9 and Table 1, as the polarization time at 4.5 is longer, the following four quantities also increase: R_{film}, R_{CT}, the interfacial capacitance coupled with R_{CT} and $Z''_{\omega \to 0}$. These trends reflect pronounced changes in the structure of the electrode due to polarization at the high potential, which strongly affects the kinetics of the electrode as well. The increase in R means that the kinetics becomes sluggish, while the increase in $Z''_{\omega \to 0}$ means a decrease in the electrode's capacity, which is the direct result of the fading mechanism at 4.5 V. The increase in C interfacial (Table 1) probably indicates an increase in the porosity of the active mass due to dissolution of Mn (as discussed already above).

The last piece of information was obtained from PITT from which the diffusion time, τ, is calculated: $\tau = l^2/D$ (with l = diffusion length and D = chemical diffusion coefficient) is equal to $(Q_t \Delta x/\pi^{1/2} I t^{1/2})^2$ at $t \ll \tau$ (the Cottrell region), where Q_t is the total intercalation capacity and Δx is the specific intercalation step.

The diffusion time τ can also be calculated from EIS, as it is equal to $(\sqrt{2} Q_t A_w \mathrm{d}X/\mathrm{d}E)^2$, where A_w is the 'Warburg' slope and $\mathrm{d}X/\mathrm{d}E$ can be obtained from SSCV at very slow scan rates.

Fig. 10 shows the plots of τ vs. E calculated from PITT for both spinel A and B electrodes. It should be emphasized that similar results were obtained by parallel calculations of τ from EIS.

The τ vs. E curves for both electrodes are similar and have peaks at the CV peak potentials. Since D is l^2/τ, D vs. E for both electrodes, is also a peak shaped function with minima at the CV peak potentials.

As already explained [11–13], such a non-monotonous, peak shaped behavior of τ and D vs. E is typical of insertion processes in which strong attractive interactions exist amongst the insertion sites, and for processes in which phase transition is involved.

As shown in Fig. 10, τ for $Li_xMn_2O_4$ A is about 4–5 times larger than that for $Li_xMn_2O_4$ B. Assuming the same values of D for both materials, and the fact that the particle size of the former material is 4–5 times bigger than that of the latter one (see Section 2, results from SEM and BET analysis), we would expect τ for $Li_xMn_2O_4$ A to be 25 times larger than that of $Li_xMn_2O_4$ B (as $\tau = l^2/D$). Hence, these results reflect (as expected) that larger particles have a larger diffusion length, and that the important factor which determines the diffusion length for these insertion electrodes is not the electrode's thickness but rather the particle size [11–13].

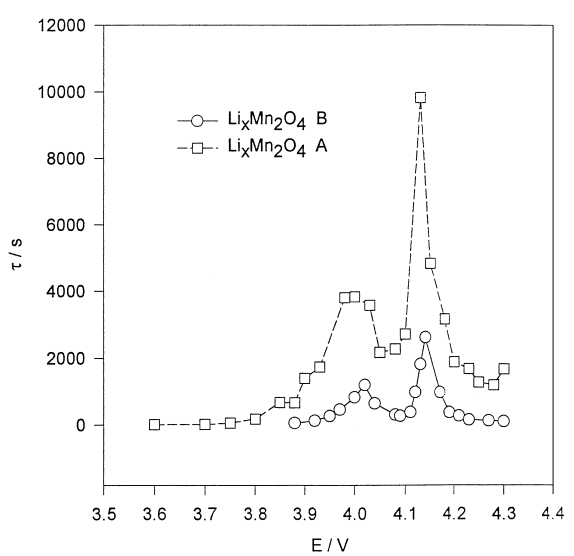

Fig. 10. Diffusion time τ as a function of E calculated for $Li_xMn_2O_4$ A and B electrodes (as indicated) from PITT.

We assume that because large particles should have more cracks and imperfections than small particles, the actual effective diffusion length is smaller than half of the geometric particle size.

The similarities in the behavior of τ and D vs. E for the two electrodes during Li insertion–deinsertion in the 3.5–4.2 V range converge with the similarities in their impedance behavior in the same potential range.

4. Conclusion

The performance of $Li_xMn_2O_4$ electrodes is strongly dependent on their preparation mode and the resulting morphology of the active mass (e.g., particle size, surface area porosity). We discovered two types of capacity fading mechanisms for $Li_xMn_2O_4$ electrodes prepared by processes differing from each other in the starting materials and in the heating and cooling programs (involving heating up to 750°C for both materials). One mechanism involves loss of about one third of the initial capacity during the first Li deintercalation–intercalation cycle in the 3.5–4.2 V range. A new, less symmetric and more disordered phase is thus formed (evident from the in situ and ex situ XRD), probably close to the surface of the active mass. However, this new, inactive mass does not considerably influence the kinetics of the remaining active mass (as evident from EIS, D vs. E and SSCV).

Another capacity fading mechanism occurs at elevated potentials (> 4.4 V vs. Li/Li^+). It involves dissolution of manganese, which is accelerated by parallel oxidation of the solution which occurs at a low rate in this potential range. This capacity fading mechanism also leads to a pronounced increase in the electrode's impedance.

Acknowledgements

Partial support for this work was obtained from the BMBF, the German Ministry of Science, and Merck (Darmstadt, Germany).

References

[1] W. Liu, K. Wowal, G.C. Farrington, J. Electrochem. Soc. 145 (1998) 459.
[2] Y.Y. Xia, M. Yoshio, J. Power Sources 66 (1997) 129.
[3] Z. Jiang, K.M. Abraham, J. Electrochem. Soc. 143 (1996) 1591.
[4] C. Sigala, A. Verbaere, J.L. Mansot, D. Guyomard, Y. Piffard, M. Tournoux, J. Solid State Chem. 132 (1997) 372.
[5] M.E. Spahr, P. Novak, O. Haas, R. Nespar, J. Power Sources 68 (1997) 629.
[6] Y. Ein Eli, W.F. Howard, S.H. Lu, S. Mukerju, J. McBrun, J.T. Vaughey, M. Thackeray, J. Electrochem. Soc. 145 (1998) 1238.
[7] A. de Koch, E. Ferg, R.J. Gummow, J. Power Sources 70 (1998) 247.
[8] F. Lecras, M. Anne, D. Bloch, P. Strobel, Solid State Ionics 106 (1998) 1.
[9] Y. Xia, Y. Zhou, M. Yoshio, J. Electrochem. Soc. 144 (1997) 2593.
[10] G. Pistoia, A. Antonini, R. Sosati, D. Zane, Electrochim. Acta 41 (1996) 2683.
[11] M.D. Levi, D. Aurbach, J. Phys. Chem. B 101 (1997) 4630, 4641.
[12] M.D. Levi, D. Aurbach, J. Electroanal. Chem. 421 (1997) 79, 89.
[13] D. Aurbach, M.D. Levi, G. Salitra, B. Markovsky, H. Teller, U. Heider, L. Heider, J. Electrochem. Soc. 145 (1998) 3024.
[14] D. Aurbach, M.D. Levi, E. Levi, A. Schechter, J. Phys. Chem. B 101 (1997) 2195.
[15] D. Aurbach, M. Moshkovich, A. Schechter, B. Markovski, M.D. Levi, Y. Cohen, New insights into the interactions between electrode materials and electrolyte solutions for advanced nonaqueous batteries, J. Power Sources, the Proceedings of the 9ILMB, 1998, submitted.
[16] Y. Gao, J.R. Dahn, Solid State Ionics 84 (1996) 33.
[17] D. Guyomard, J.M. Tarascon, Solid State Ionics 69 (1994) 222.